

Article

Coordinated Slip Control of Multi-Axle Distributed Drive Vehicle Based on HLQR

Yutong Bao ^{1,2,3}, Changqing Du ^{1,2,3} , Dongmei Wu ^{1,2,3,*}, Huan Liu ^{1,2,3}, Wei Liu ⁴ and Jun Li ⁵

¹ Hubei Key Laboratory of Advanced Technology for Automotive Components, Wuhan University of Technology, Wuhan 430070, China; 216705@whut.edu.cn (Y.B.); cq_du@whut.edu.cn (C.D.); 292965@whut.edu.cn (H.L.)

² Foshan Xianhu Laboratory of the Advanced Energy Science and Technology Guangdong Laboratory, Foshan 528200, China

³ Hubei Research Center for New Energy & Intelligent Connected Vehicle, Wuhan University of Technology, Wuhan 430070, China

⁴ School of Electrical and Computer Engineering, Purdue University, West Lafayette, IN 47907, USA; liu3044@purdue.edu

⁵ Tsinghua Intelligent Vehicle Design and Safety Research Institute, Tsinghua University, Beijing 100084, China; junli@tsinghua.edu.cn

* Correspondence: wudongmei@whut.edu.cn

Abstract: For multi-axle distributed drive (MADD) vehicles, the complexity of the longitudinal dynamics control system increases with the number of driven wheels, which presents a huge challenge to control the multi-motor drive vehicle with more than four wheels. To reduce the control system complexity, this paper proposes a coordinated slip control algorithm using the hierarchical linear quadratic regulator (HLQR) scheme for a 12×12 MADD vehicle. The 12-wheel driving system is decoupled based on the wheel load and simplified to a double local subsystem. First, the 12×12 MADD vehicle dynamics model is established. Then, the optimal slip ratio is obtained on the basis of the road friction coefficient estimation through a fuzzy control algorithm when the wheel slips. Afterwards, the wheel slip ratio is controlled based on the HLQR program for anti-slip regulation. Furthermore, the driving torque control allocation based on quadratic programming (QR) is coordinated with the anti-slip control. Simulink results show that the proposed coordinated slip control based on HLQR can improve slip control accuracy by more than 30% and greatly reduce the calculation load. The torque control allocation is also limited by the slip control results to ensure wheel dynamic stability and smoothly satisfy the driver's demand.

Keywords: distributed drive; multi-axle vehicle; slip ratio control; hierarchical linear quadratic regulator; torque distribution

MSC: 90C20



Citation: Bao, Y.; Du, C.; Wu, D.; Liu, H.; Liu, W.; Li, J. Coordinated Slip Control of Multi-Axle Distributed Drive Vehicle Based on HLQR. *Mathematics* **2023**, *11*, 1964. <https://doi.org/10.3390/math11081964>

Academic Editor: Jinfeng Liu

Received: 22 January 2023

Revised: 6 April 2023

Accepted: 18 April 2023

Published: 21 April 2023



Copyright: © 2023 by the authors. Licensee MDPI, Basel, Switzerland. This article is an open access article distributed under the terms and conditions of the Creative Commons Attribution (CC BY) license (<https://creativecommons.org/licenses/by/4.0/>).

1. Introduction

With the booming development of modern highways, large special vehicles as well as heavy vehicles have become the main means of transportation for large equipment or a large amount of materials. Multi-axle drive patterns with more than two axles can significantly increase the load capacity of the vehicle, which is an important trend in the development of heavy vehicles [1]. Furthermore, hybrid electric vehicles (HEVs) and electric vehicles (EVs) are regarded as one approach to solving the problems of the global environment and energy, which also facilitate the realization of autonomous driving [2–4]. In addition, the electric motor driving system can generate torque faster and more accurately than the international combustion engine (ICE). In particular, distributed-drive EVs can control the wheel braking/driving torque independently, which is greatly beneficial for vehicle longitudinal and lateral dynamics control [5–7]. In particular, the distributed drive system is suitable for commercial multi-axle driven vehicles, where the problems of the

layout and the increased unsprung mass are not as obvious as in passenger cars [8–10]. Therefore, multi-axle distributed drive (MADD) vehicles have been the focus of researchers. Previous studies have indicated the performance improvement of MADD vehicles in traction, steering response, and yaw stability [11,12].

Anti-skid control is essential for vehicle longitudinal dynamics control to improve vehicle stability [13–15]. For MADD vehicles, the driving torque can be flexibly distributed among the wheels. In summary, there are two layers of control in longitudinal dynamics: (1) the upper-level controller focuses on the control allocation between the wheel torques; and (2) the lower-level controller regulates the torque driven on the wheel based on the slip ratio control. In the control allocation of MADD vehicles, multi-objective optimization methods are usually used to satisfy the vehicle control requirements in several aspects [16,17]. The control objectives generally include the minimum following error of the total desired torque, the additional yaw moment, and the minimum consumption of road friction conditions. Other factors related to electric motor failure, such as the limit of the torque output and the energy consumption, can also be integrated into the control objective [18]. Quadratic programming (QP) is widely employed for the formulation of multi-objective optimization problems [19,20]. After solving the above problem, the desired torque for each wheel is obtained for the lower driving torque control layer.

In the layer of driving torque control for each wheel, slip-based control is common. Slip ratio is an important variable to control the tire force by regulating the wheel driving torque [21,22]. Various control methods have been applied for slip control, such as the proportional integral derivative (PID) method, the sliding mode control (SMC) algorithm, and the model predictive control (MPC) scheme [23,24]. If the slip ratio is too large, the driving torque should be regulated to reduce wheel spinning. In this condition, the wheel slip ratio with the maximum driving force is usually set as the reference slip ratio [25,26]. However, anti-slip control and torque distribution control are usually realized independently. If the wheel is determined to be a slipping wheel, the driving torque is reduced directly in the low layer of the torque control. Actually, the state of the wheel slipping should be considered in the torque control allocation. For instance, the driving torque can be transferred to other wheels if one of the wheels reaches a large slip ratio.

In previous studies, slip ratio control was generally conducted individually for each wheel, where the single-input and single-output (SISO) methods, such as PID and SMC, were usually used [5,16]. These methods control the slip ratio of each wheel, which is treated as a local subsystem of the vehicle. This way, every local subsystem can be stabilized. However, it cannot ensure the global stability of the vehicle. As a result, the multi-input and multi-output (MIMO) control methods, such as the linear quadratic regulator (LQR) method, should be designed to stabilize the overall system. However, the dimensions of the control system will be larger when there are more driven wheels. As there are physical interactions among the wheels because of the mechanical connections between the wheels and the vehicle body, the MADD vehicle should be treated as a multiagent dynamical system [27]. For the multiagent system, the hierarchical linear quadratic regulator (HLQR) is an alternative proposed solution for optimal control of the complex dynamical system [28]. It aims to simplify the control model through the control of the representative local subsystem according to the internal connections. In reference [29], the HLQR is applied for slip control of a four-wheel independently driven vehicle, where the parameters and the movement of each wheel are assumed to be almost the same.

However, for MADD vehicles with more than four wheels, the vehicle length and distances between axles increase, which will increase the difference in parameters and rotation states between wheels. Thus, the multiagent system cannot be simplified to several same local subsystems. Multi-wheels must be classified and decoupled according to their physical characteristics. Furthermore, there are more control variables, and the coupling of wheels will be more complex for MADD vehicles, which makes it difficult to construct the HLQR system. Nevertheless, this is where HLQR can leverage its strengths. If HLQR is successfully implemented, the complexity of the control system will be significantly

reduced. Therefore, the construction and application of the HLQR system for MADD vehicles with more than four wheels must be further explored.

As the previous research about HLQR for four-wheel in-wheel-motor vehicles is not suitable for MADD vehicles with more than two axles. This research gives a solution for simplifying the longitudinal dynamics control for a 12×12 MADD vehicle based on HLQR. As the wheel rotation speed and slip ratio are affected by the wheel load, the wheel load is one of the most important physical characteristics of each wheel. Even though the instantaneous dynamic wheel load changes with the load transformation as the vehicle drives, it is related to the static wheel load, which depends on the distance between axles. Thus, this paper decouples the 12 wheels based on the wheel static load and divides the 12×12 driving system into two local subsystems. Subsequently, this paper shows that HLQR is realized by a hierarchical control framework. The lower level for each subsystem tracks the reference slip ratio with the maximum driving coefficient when the wheel slips. The upper level obtains the driving torque for all wheels according to the interconnection between the two subsystems. In this way, the calculation of the slip control system for 12 wheels can be considerably simplified. In addition, the driving torque control allocation based on the QP algorithm makes wheel slipping a constraint, where the state of wheel slipping can be fed back to the upper layer for torque distribution. This facilitates the collaboration of slip ratio control and torque distribution.

In summary, the main contributions of this paper are as follows:

- (1) The HLQR method is expanded to a 12×12 MADD vehicle, where the 12-wheel driving system is decoupled according to the static wheel load and simplified to a double local subsystem. The front four wheels with a small vertical load are simplified to a local system, and the rear eight wheels with a large vertical load are simplified to another local system. The complexity of the longitudinal dynamics system for 12 wheels is reduced significantly;
- (2) The coordination of anti-slip control and torque distribution is proposed. By adopting the wheel-slipping state as a constraint, the torque distribution can be regulated based on the feedback.

The following sections of this paper are described: in Section 2, the longitudinal dynamics control framework and vehicle dynamics modeling for MADD vehicles are introduced. Then, in Section 3, the HLQR method is utilized for the anti-slip control of wheels. In Section 4, the torque distribution control of the vehicle is coordinated with the slip control based on the QP algorithm. In Section 5, some cases are simulated to verify the proposed algorithm. Section 6 demonstrates the discussions.

2. Control Framework and MADD Vehicle Model

2.1. Framework of Coordinated Slip Control

The framework of the coordinated slip control is presented in Figure 1. There are two control layers: the slip control based on HLQR and the coordinated control of anti-slip and torque distribution. First, slip control based on HLQR is conducted to ensure the stability of each wheel. If the wheel is recognized to be slipping, the slip ratio that the extreme driving coefficient reaches is set to the optimal slip ratio. According to the HLQR control scheme, the control system with 12 wheels is divided into a dual local subsystem. In this way, the anti-slip control problem of 12 wheels is simplified and solved to follow the optimal slip ratio. Then, to distribute the torque among the 12 wheels, the coordinated control of anti-slipping and torque allocation is assigned. When anti-skid control is involved, the torque of the slipping wheel is constrained by the slip control. The torque of the other wheels can be redistributed to ensure the overall drive's performance and stability.

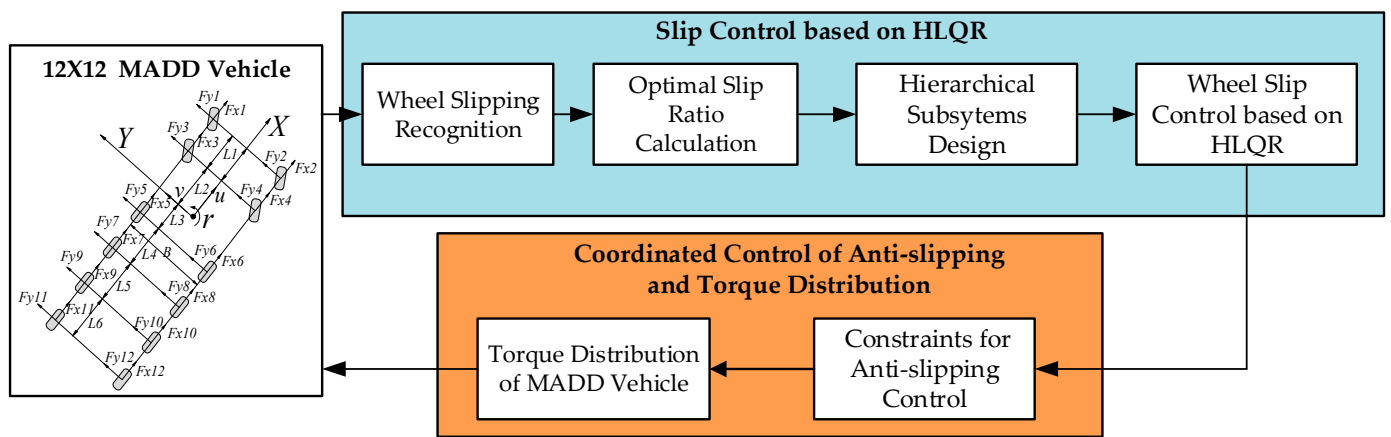


Figure 1. The coordinated slip control framework of the MADD vehicle.

2.2. Modeling of the MADD Vehicle

This paper focuses on a 12×12 HEV, which consists of an auxiliary power unit (APU) and 12-wheel-side electric motors in the driving system. The APU generates electric power from a diesel engine. The wheels are driven independently by the 12 electric motors. As the aim of this paper is vehicle dynamics control in the longitudinal direction, the power system is ignored, and only the dynamics model of the MADD vehicle is established. For coordinated slip control, the MADD vehicle dynamics model in the longitudinal, lateral, and yaw directions is developed as shown in Figure 2.

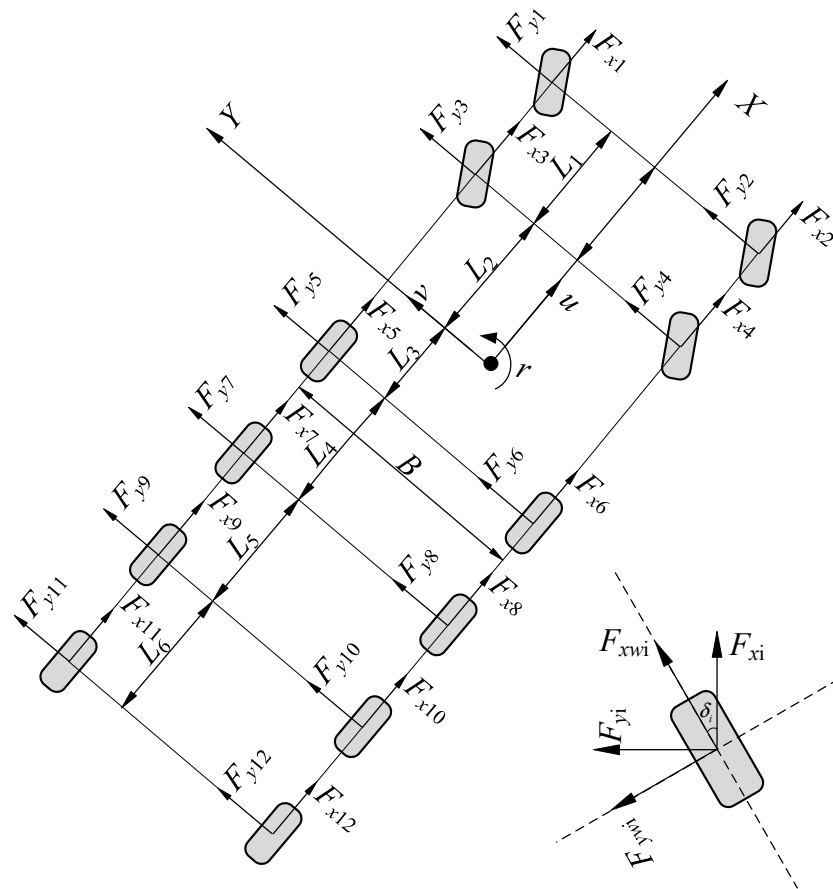


Figure 2. Dynamics model of the 12×12 MDDD vehicle.

The specific model of the 12 × 12 MADD vehicle in the longitudinal direction, lateral direction, and yaw direction are presented as (1):

$$\begin{cases} m(\dot{u} - rv) = \sum_{i=1}^{12} F_{xi} - F_R \\ m(\dot{v} + ru) = \sum_{i=1}^{12} F_{yi} \\ I_z \dot{r} = (L_1 + L_2)(F_{y1} + F_{y2}) + L_2(F_{y3} + F_{y4}) - L_3(F_{y5} + F_{y6}) \\ \quad - (L_3 + L_4)(F_{y7} + F_{y8}) - (L_3 + L_4 + L_5)(F_{y9} + F_{y10}) \\ \quad - (L_3 + L_4 + L_5 + L_6)(F_{y11} + F_{y12}) + \frac{B}{2} \sum_{i=2}^{12} F_{xi} - \frac{B}{2} \sum_{j=1}^{11} F_{xj} \end{cases} \quad (1)$$

where m is the vehicle mass; u is the vehicle speed in longitudinal direction; v is the vehicle lateral velocity; r is the yaw rate; F_{xi} and F_{yi} are the longitudinal and lateral forces of wheel i under the vehicle coordinate system; F_R is the driving resistance consisting of rolling resistance, acceleration resistance, and slope resistance; and L_1, L_4, L_5 and L_6 are the distances between one axle and the next axle, as shown in Figure 2. L_2 and L_3 are the distances from the 2nd and 3rd axles to the center of mass, respectively, and I_z is the vehicle yaw rotational inertia. B is the wheel base.

The rotational motion of the wheel can be modeled by the following equation:

$$I_w \frac{d\omega_i}{dt} = T_i i_g - T_{bi} - T_{fi} - F_{xwi} \cdot r_w \quad (2)$$

where I_w is the wheel rotational inertia, ω_i is the rotation speed of wheel i , T_i is the drive torque on wheel i , i_g is the gear ratio, T_{bi} is the wheel braking torque, F_{zwi} is the wheel vertical load, T_{fi} is the rolling resistance, F_{xwi} is the wheel driving force under the wheel coordinate system, and r_w is the tire radius.

The Dugoff tire model is adapted to calculate the tire force in longitudinal direction F_{xwi} and the tire force in lateral direction F_{ywi} . This model can be applied for the condition with combined slipping in the longitudinal direction and lateral direction [30]. The presentation of the tire forces is given in (3):

$$\begin{cases} F_{xwi} = C_x \cdot \frac{S_{xi}}{1+S_{xi}} f(\lambda) \\ F_{ywi} = C_y \cdot \frac{\tan \alpha}{1+S_{xi}} f(\lambda) \\ f(\lambda) = \begin{cases} \lambda(2 - \lambda) & \lambda \leq 1 \\ 1 & \lambda > 1 \end{cases} \\ \lambda = \frac{\mu F_{zwi}(1+S_{xi})}{2\sqrt{(C_x S_{xi})^2 + (C_y \tan \alpha)^2}} \end{cases} \quad (3)$$

where C_x and C_y are the longitudinal and lateral stiffness of the tire, S_{xi} is the longitudinal slip/rotation ratio, and α is the side slip angle of the tire. λ is the parameters to judge whether the current working state of the tire is in the linear zone, and μ is the peak adhesion coefficient of the road surface.

The calculation of the tire slip ratio can be conducted using the following equation:

$$S_{xi} = \frac{\omega_i r_{wi} - u_{wi}}{\max(\omega_i r_{wi}, u_{wi})} \quad (4)$$

where u_{wi} is the wheel moving speed, which can be approximated as the vehicle speed [31].

3. Slip Control Based on HLQR

For anti-slipping control, the optimal output torque of every single wheel is calculated to track the optimal slip ratio. On the basis of the HLQR scheme, the time-varying inter-connection system with 12 wheels is reconstructed into dual local subsystems, which can simplify the calculation of the control algorithm.

3.1. Calculation of the Optimal Slip Ratio

For antiskid control, the optimal slip ratio is generally defined as the slip ratio that can reach the maximum driving force coefficient, which is related to the road adhesion coefficient. In this paper, the optimal slip ratio is determined by a fuzzy control algorithm based on road identification. For the MADD vehicle researched in this paper, Figure 3 shows the relationship between the driving coefficient and the wheel slip ratio on the road surface with an adhesion coefficient of 1.0. The extreme driving coefficient is at its maximum at the optimal slip ratio.

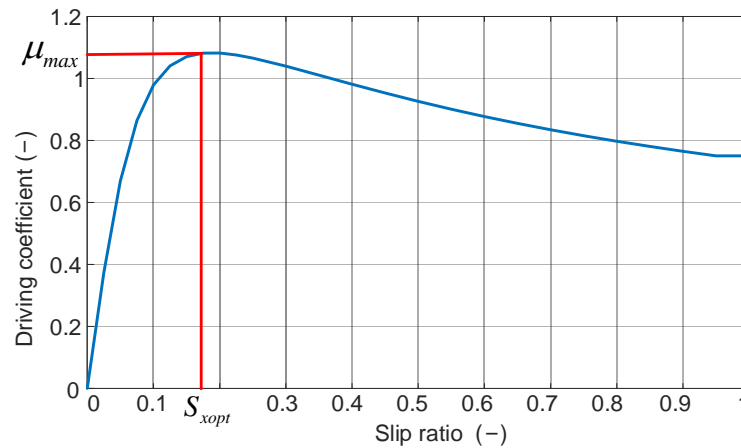


Figure 3. Driving coefficient on road surface with adhesion coefficient of 1.0.

The relationship between the driving coefficient μ and the wheel slip ratio S_{xi} of the wheel i shown in Figure 3 can be written as the following equation [32]:

$$\begin{cases} \mu(S_{xi}) = C_1(1 - e^{-c_2 S_{xi}}) - C_3 S_{xi} \\ S_{xiopt} = \frac{1}{C_2} \ln \frac{C_1 C_2}{C_3} \\ \mu_{max} = C_1 - \frac{C_3}{C_2} (1 + \ln \frac{C_1 C_2}{C_3}) \end{cases} \quad (5)$$

where C_1, C_2, C_3 are the constant parameters of the road surface, S_{xiopt} is the optimal slip ratio of wheel i on the present road surface, and μ_{max} is the adhesion coefficient. The parameters of different road surfaces are referred to in the literature [32].

The fuzzy method is adopted to identify the present road surface and obtain the optimal slip ratio. The inputs of the fuzzy control method are the current slip ratio, wheel driving force, and wheel vertical load. In this way, the road can be identified, and the corresponding optimal slip ratio can be obtained.

3.2. Modeling of MADD Driving System

For the linear quadratic regulator (LQR) problem, it is necessary to build the wheel dynamics model with the slip ratio as a state variable. For driving conditions, the derivative of the slip ratio (6) can be obtained based on (4):

$$\dot{S}_{xi} = -\frac{1}{r_w} \cdot \frac{\dot{u}\omega_i - u\dot{\omega}_i}{\omega_i^2} \quad (6)$$

According to (1), (2), (4) and (7) can be derived as follows:

$$\begin{cases} \sum_{i=1}^{12} I_{wi}\dot{\omega}_i = \sum_{i=1}^{12} T_i - \sum_{i=1}^{12} T_{fi} - r_w \cdot \sum_{i=1}^{12} F_{xi} \\ \dot{u} = \frac{1}{mr_w} (\sum_{i=1}^{12} T_i - \sum_{i=1}^{12} T_{fi} - \sum_{i=1}^{12} I_{wi}\dot{\omega}_i - r_w \cdot F_R) \\ u = (1 - S_{xi})\omega_i r_w \end{cases} \quad (7)$$

Assuming that the rolling resistance can be ignored, the dynamics model of the wheel slip ratio can be solved by substituting (7) into (6):

$$\dot{S}_{xi} = -\frac{r_w}{I_{wi}\omega_i}F_{xwi} - \frac{1}{m\omega_i r_w} \sum_{i=1}^{12} F_{xwi} - \frac{\dot{\omega}_i}{\omega_i} S_{xi} + \frac{1}{I_{wi}\omega_i} T_i \tag{8}$$

By defining $\dot{e}_i = S_{xi} - S_{xiopt}$, $\mathbf{x}_i = [F_{xwi}, S_{xi}, e_i]^T$ and $u_i = T_i$, the state equation of each wheel can be expressed as follows:

$$\dot{\mathbf{x}}_i = \mathbf{A}_{1i}\mathbf{x}_i + \sum_{i=1}^{12} \mathbf{A}_{2i}\mathbf{x}_i + \mathbf{B}_{1i}u_i + \mathbf{B}_{2i}S_{xiopt} \tag{9}$$

where

$$\mathbf{A}_{1i} = \begin{bmatrix} -\frac{1}{T_{ni}} & \frac{C_{xi}}{T_{ni}} & 0 \\ -\frac{r_w}{I_{wi}\omega_i} & -\frac{\omega_i}{\omega_i} & 0 \\ 0 & 1 & 0 \end{bmatrix} \tag{10}$$

$$\mathbf{A}_{2i} = \begin{bmatrix} 0 & 0 & 0 \\ -\frac{1}{m\omega_i r_w} & 0 & 0 \\ 0 & 0 & 0 \end{bmatrix} \tag{11}$$

where $\mathbf{B}_{1i} = [0 \quad \frac{1}{I_{wi}\omega_i} \quad 0]^T$, $\mathbf{B}_{2i} = [0 \quad 0 \quad -1]^T$ and T_{ni} is the inertia time constant of the tire force.

Based on (9), the whole driving system with 12 wheels can be expressed in (12):

$$\dot{\mathbf{X}} = \mathbf{A}\mathbf{X} + \mathbf{B}\mathbf{U} + \mathbf{D}_t \tag{12}$$

where $\mathbf{X} = [x_1, x_2, \dots, x_{12}]^T$, $\mathbf{U} = [u_1, u_2, \dots, u_{12}]^T$, $\mathbf{A} = \mathbf{I}_{12} \otimes \mathbf{A}_{1i} + \mathbf{\Gamma}_{12}\mathbf{A}_{2i}$ and $\mathbf{B} = \mathbf{I}_{12} \otimes \mathbf{B}_{1i}$.

Where \mathbf{I}_{12} is the identity matrix with 12 rows and 12 columns, and $\mathbf{\Gamma}_{12}$ is the matrix with full 1 for 12 rows and 12 columns. As \mathbf{B}_{2i} and S_{xiopt} are constant on the same road surface, $\mathbf{D}_t = \mathbf{I}_{12} \otimes \mathbf{B}_{2i} \cdot S_{xiopt}$ can be seen as the external interference term.

3.3. Design of the HLQR Control System

The multiple wheels have essentially the same dynamics and interact with each other, which can be described as a multibody interconnected system. Based on the HLQR control scheme for this type of system, the whole control system includes the upper layer and the lower layer, as shown in Figure 4. In the lower layer, the local feedback gains \mathbf{K}_1 can be obtained based on the solution of the Riccati equation for the local homogeneous system. For the upper layer, the upper feedback gain \mathbf{K}_g is solved by considering the interconnection of multiple local systems. The control outputs of both layers are added up to calculate the control input of the whole system $\mathbf{U}(t)$.

For the system with 12 wheels, the optimal feedback gain of the whole control system can be calculated as follows:

$$\mathbf{K} = \mathbf{I}_{12} \otimes \mathbf{K}_1 + \mathbf{\Gamma}_{12} \otimes \mathbf{K}_g \tag{13}$$

where \mathbf{K}_1 is the feedback gains of the local homogeneous system, \mathbf{K}_g is the overall feedback gain, and \otimes is the Kronecker product.

The feedback gains \mathbf{K}_1 and \mathbf{K}_g can both be solved according to the LQR theory, as shown in (14):

$$\begin{cases} \mathbf{K}_1 = \mathbf{R}_1^{-1}\mathbf{B}_{11}^T\mathbf{P}_1 \\ \mathbf{K}_g = \mathbf{R}_g^{-1}\mathbf{B}_{11}^T\mathbf{P}_1 \end{cases} \tag{14}$$

where \mathbf{P}_1 is the Riccati equation solution of the local subsystems, \mathbf{R}_1 is the weight matrix of the control input of the local subsystem, and \mathbf{R}_g is the weight matrix of the global control input considering the interconnection between subsystems.

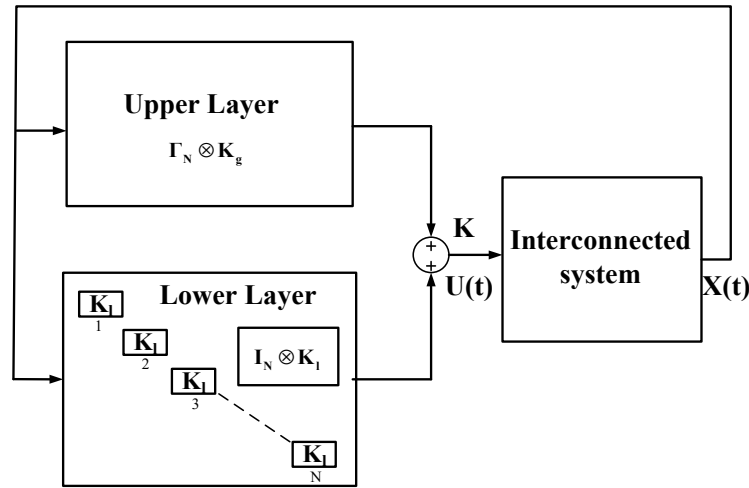


Figure 4. HLQR for a single wheel of the MADD vehicle.

The Riccati equation solution \mathbf{P}_1 of the local subsystems can be obtained by the following equation:

$$\dot{\mathbf{P}}_1 = -\mathbf{P}_1\mathbf{A}_{1i} - \mathbf{A}_{1i}^T\mathbf{P}_1 + \mathbf{P}_1\mathbf{B}_{1i}\mathbf{R}_1^{-1}\mathbf{B}_{1i}^T\mathbf{P}_1 - \mathbf{Q}_1 \tag{15}$$

where \mathbf{Q}_1 is the weight matrix of the state variable of the local subsystem.

For the 12×12 MADD vehicle researched in this paper, the vertical load on the front four wheels is considerably greater than that on the eight rear wheels. In addition, the longitudinal stiffness of the front four wheels is also substantially higher than that of the rear eight wheels. Therefore, the working conditions of the wheels on the front two axles are different from those of the wheels on the rear four axles at the same time. As a result, the whole system with 12 wheels can be divided into two local subsystems. The first one is represented by the left wheel of the 1st axle, and the second one is represented by the left wheel of the 3rd axle.

The whole feedback gain can be described as follows:

$$\mathbf{K} = \begin{bmatrix} \mathbf{I}_{4 \times 4} \otimes \mathbf{K}_{11} & \mathbf{0}_{4 \times 8} \\ \mathbf{0}_{8 \times 4} & \mathbf{I}_{8 \times 8} \otimes \mathbf{K}_{15} \end{bmatrix} + [\mathbf{\Gamma}_{12 \times 4} \otimes \mathbf{K}_{g1} \quad \mathbf{\Gamma}_{12 \times 8} \otimes \mathbf{K}_{g5}] \tag{16}$$

where $\mathbf{K}_{11} = \mathbf{R}_{11}^{-1}\mathbf{B}_{11}^T\mathbf{P}_{11}$, $\mathbf{K}_{g1} = \mathbf{R}_{g1}^{-1}\mathbf{B}_{11}^T\mathbf{P}_{11}$, $\mathbf{K}_{15} = \mathbf{R}_{15}^{-1}\mathbf{B}_{15}^T\mathbf{P}_{15}$, $\mathbf{K}_{g5} = \mathbf{R}_{g5}^{-1}\mathbf{B}_{15}^T\mathbf{P}_{15}$, \mathbf{P}_{11} and \mathbf{P}_{15} are calculated by the solution of the Riccati equation.

It can be seen that \mathbf{B}_{11} , \mathbf{B}_{15} are both matrix with 3×1 dimensions, the Hamiltonian matrix is a 6×6 matrix. However, the matrix \mathbf{A} in the whole system model has dimensions of 36×36 . As a result, with the HLQR control, the calculation load of the slip control is reduced immensely.

For each local subsystem, a standard quadratic objective function is constructed in a control step $T_s = [t_0 \ t_f]$ as follows:

$$J = \frac{1}{2}\mathbf{X}_t^T\mathbf{S}\mathbf{X}_t + \int_{t_0}^{t_f} (\frac{1}{2}\mathbf{X}^T\mathbf{Q}\mathbf{X} + \frac{1}{2}\mathbf{U}^T\mathbf{R}\mathbf{U})dt \tag{17}$$

where \mathbf{S} , \mathbf{Q} , \mathbf{R} are the weight matrices, $\mathbf{U} = -\mathbf{K}\mathbf{X}$.

Specifically, the HLQR problem can be solved by the following steps, as shown in Algorithm 1.

Algorithm 1: HLQR Algorithm

Initialization: Configure weight matrix $\mathbf{Q}_{11}, \mathbf{Q}_{15}, \mathbf{R}_{11}, \mathbf{R}_{15}, \mathbf{R}_{g1}, \mathbf{R}_{g5}$ and Initialize $\mathbf{S}_{11}, \mathbf{S}_{15}$;

Calculation: Calculate the state transition matrix $\mathbf{A}_{11}, \mathbf{A}_{15}$ and control matrix $\mathbf{B}_{11}, \mathbf{B}_{15}$ of two local subsystems;

Analytical solution: Constructing Hamiltonian matrices of two local subsystems, $t = t_0$,
 $t_f - t_0 = T_s = 0.01$ s, obtain the Riccati equation analytical solution
 $\mathbf{P}_{11}, \mathbf{P}_{15}$ respectively;

Control output: Find the global optimal feedback gain \mathbf{K} and the optimal control input \mathbf{U} ;

Repeat: $\mathbf{S}(k + 1) = \mathbf{P}(t_f, k - 1) = \mathbf{P}(t_0, k - 1)$;

Return: \mathbf{A}, \mathbf{B} .

4. Torque Control Allocation Based on QP

Through slip control in Section 3, the driving force of each wheel is regulated to prevent large wheels from slipping. According to the characteristics of MADD vehicles, the driving torque needs to be further distributed among individual wheels according to the slip control of every single wheel. In this paper, the QP algorithm is adopted for torque control allocation, where the wheel slip control results are taken as a constraint.

4.1. Cost Function of Torque Control Allocation Problem

The cost function includes three items are as follows:

$$\mathbf{f}(\mathbf{x}) = \lambda^2 \mathbf{f}_1 + \sigma^2 \mathbf{f}_2 + \kappa^2 \mathbf{f}_3 \tag{18}$$

where $\mathbf{x} = [x_{_1}, x_{_2}, \dots, x_{_12}]^T = [F_{x1}, F_{x2}, \dots, F_{x12}]^T$, $\mathbf{f}_1, \mathbf{f}_2$, and \mathbf{f}_3 are the three objective items and λ, σ, κ are the weight factor of the three objective items.

Every cost function term can be formulated as a QP problem. The first term of the objective function is the tracking error of the demand driving force and the additional yaw moment:

$$\lambda^2 \mathbf{f}_1 = \frac{1}{2} \mathbf{x}^T \mathbf{H}_{11} \mathbf{x} + \mathbf{c}_{11}^T \mathbf{x} + \frac{1}{2} \mathbf{x}^T \mathbf{H}_{12} \mathbf{x} + \mathbf{c}_{12}^T \mathbf{x} \tag{19}$$

where $\mathbf{H}_{11} = 2\lambda^2 W_{F_x}^2 \cdot \mathbf{\Gamma}_{12}, \mathbf{c}_{11} = -2\lambda^2 W_{F_x}^2 F_{x_need} \cdot \mathbf{\Gamma}_{12}^T, M_{z_need}$ is the desired additional yaw moment arising from the differential driving control, $\mathbf{h}_{12_part} = [1 \quad -1 \quad \dots \quad 1 \quad -1]_{1 \times 12}$, $\mathbf{h}_{12} = [\mathbf{h}_{12_part} \quad -\mathbf{h}_{12_part} \quad \dots \quad \mathbf{h}_{12_part} \quad -\mathbf{h}_{12_part}]_{12 \times 12}, \mathbf{H}_{12} = 2\lambda^2 (\frac{B}{2} W_{M_z})^2 \cdot \mathbf{h}_{12}$, $\mathbf{c}_{12} = -2\lambda^2 W_{M_z}^2 \frac{B}{2} M_{z_need} \cdot \mathbf{h}_{12}^T$, B is the wheelbase, W_{F_x}, W_{M_z} are the weight factors about the tracking error of the F_{x_need} and the M_{z_need} , respectively.

The second item of the objective function aims to ensure the utilization of the road adhesion condition. By minimizing the adhesion utilization coefficient, the drag force between the tire and the road can be guaranteed, which is beneficial for preventing wheel slipping. The second item of the objective function can be expressed as follows:

$$\sigma^2 \mathbf{f}_2 = \frac{1}{2} \mathbf{x}^T \mathbf{H}_2 \mathbf{x} + \mathbf{c}_2^T \mathbf{x} \tag{20}$$

where $\mathbf{H}_2 = 2\sigma^2 W_{\mu}^2, \mathbf{c}_2 = \mathbf{0}_{12 \times 1}, \mathbf{W}_{\mu} = \mathbf{diag}(\frac{1}{F_{z1}}, \frac{1}{F_{z2}}, \dots, \frac{1}{F_{z12}})$.

The third term of the function is according to torque redistribution when the failure of certain electric motors occurs. Additionally, it can be transformed into the quadratic form as shown in (21):

$$\kappa^2 \mathbf{f}_3 = \frac{1}{2} \mathbf{x}^T \mathbf{H}_3 \mathbf{x} + \mathbf{c}_3^T \mathbf{x} \tag{21}$$

where $\mathbf{H}_3 = 2\sigma^2\mathbf{W}_e^2$, $\mathbf{c}_3 = \mathbf{0}_{12 \times 1}$, $\mathbf{W}_e = \text{diag}(\frac{1}{e_1 F_{x1\max}}, \frac{1}{e_2 F_{x2\max}}, \dots, \frac{1}{e_{12} F_{x12\max}})$, e_i is the failure factor of each drive motor, and $F_{xi\max}$ is the drive force that can be exerted at the maximum torque of each drive motor.

4.2. Constraints for Coordinated Control with HLQR

To indicate the wheel slipping state, a flag F_{sti} is set to represent the triggering of the anti-slip control. The flag is updated using the following equation:

$$\begin{cases} F_{sti} = 1 & S_{xi} > S_{thr} \\ F_{sti} = 0 & S_{xi} < S_{thr}, \dot{F}_{x_need} < 0 \text{ and } F_{x_need} < F_{xi_ctrl} \end{cases} \quad (22)$$

where S_{thr} is the threshold of the slip ratio and F_{xi_ctrl} is the wheel longitudinal force at the moment when the anti-skid control starts.

According to (20), $F_{sti} = 1$ when the slip ratio S_{xi} is larger than the threshold value S_{thr} . This means that the anti-slip control in Section 3 is activated. To avoid frequent activation of the anti-slipping control, the flag F_{sti} is changed to zero only if three conditions are satisfied: (1) S_{xi} is smaller than the threshold value S_{thr} ; (2) the longitudinal demand force F_{x_need} is decreasing ($\dot{F}_{x_need} < 0$); and (3) the longitudinal demand force is smaller than the wheel longitudinal force at the moment when the anti-skid system is triggered by F_{x_need} ($F_{x_need} < F_{xi_ctrl}$).

When the driving wheel slips greatly, the HLQR algorithm is activated to control the slip ratio at the optimal value on the current road surface. When the slip flag F_{sti} is determined to be 1, the equality constraint is activated as follows:

$$x_i = x_{i_hlqr} \text{ if } F_{sti} = 1 \quad (23)$$

where x_{i_hlqr} is the wheel driving force controlled by the HLQR algorithm.

Combining the constraints about the maximum driving force, the failure state of the electric motor, and the change rate limit of the driving force, the constraints can be summarized by Equation (24):

$$s.t \begin{cases} x_{i_last} + \Delta x_{\min} T_s \leq x_i \leq x_{i_last} + \Delta x_{\max} T_s \\ x_i = x_{i_hlqr} \\ x_{i_hlqr} = e_i T_{\max}(\omega) \\ x_{i_hlqr} = -e_i T_{\max}(\omega) \end{cases} \quad \begin{cases} F_{sti} = 1 \\ x_{i_hlqr} > e_i T_{\max}(\omega) \\ x_{i_hlqr} < -e_i T_{\max}(\omega) \end{cases} \quad (24)$$

where Δx_{\max} and Δx_{\min} are the maximum and minimum value of the driving force change rate, respectively, and T_{\max} is the maximum wheel driving torque on the current wheel speed.

For all 12 wheels, the constraints can be expressed as follows:

$$s.t \begin{cases} \mathbf{a}_{eq}^T \mathbf{x} - \mathbf{b}_{eq} = 0 \\ \mathbf{a}_{ineq}^T \mathbf{x} - \mathbf{b}_{ineq} \geq 0 \end{cases} \quad (25)$$

where

$$\mathbf{a}_{eq} = \begin{bmatrix} F_{st1} & \dots & 0 \\ \vdots & \ddots & \vdots \\ 0 & \dots & F_{st12} \end{bmatrix} \quad (26)$$

where $\mathbf{b}_{eq} = [F_{xhlqr1} \ \dots \ F_{xhlqr12}]^T$, $\mathbf{a}_{ineq} = [diag(12, 12) \ -diag(12, 12)]_{24 \times 12}^T$, $\mathbf{b}_{ineq2} = [x_{1_last} + \Delta x_{\min} T_s \ \dots \ x_{12_last} + \Delta x_{\min} T_s - x_{1_last} - \Delta x_{\max} T_s \ \dots \ -x_{12_last} - \Delta x_{\max} T_s]_{1 \times 24}^T$, $\mathbf{b}_{ineq1} = [-e_1 T_{\max}(\omega_1) \ \dots \ -e_{12} T_{\max}(\omega_{12}) - e_1 T_{\max}(\omega_1) \ \dots \ -e_{12} T_{\max}(\omega_{12})]_{1 \times 24}^T$, x_{i_last} is the wheel driving force of the last step, e_i is failure factor, where $e_i = 0$ indicates the drive motor of the i th wheel fails completely, $e_i = 1$ indicates the drive motor of the i th wheel is normal, and $0 \leq e_i \leq 1$ indicates the drive motor of the i th wheel can only output a part of the required torque.

If the anti-slip control is not activated, e.g., $F_{sti} = 0$, the equality constraint is activated. Otherwise, the equality constraint in (25) remains empty, which means that the constraint does not work. After the formulation of the QP problem, an effective algorithm is adopted to solve the control allocation problem.

5. Simulation Results

To verify the effectiveness of the proposed control algorithm, MATLAB/Simulink combined with the TruckSim 2019.0 software is applied as the simulation platform. The 12×12 MADD vehicle model is established in TruckSim as the model of the research object. The proposed coordinated slip control algorithm runs on MATLAB/Simulink. The necessary information about the wheel and vehicle state is supplied by the vehicle model in TruckSim. The required torque of each driving motor is output by the control system in MATLAB/Simulink and sent to the vehicle model in TruckSim. Several important parameters of the vehicle model are summarized in Table 1.

Table 1. Parameters of the 12×12 MADD vehicle model.

Parameters	Value
Vehicle mass(no load) (kg)	6310
Number of driving wheel (-)	12
Rated torque of each wheel (Nm)	1100
Effective rolling radius (mm)	550
Height of mass center (mm)	1407
Distance between axles (L1–L6) (mm)	2600, 2500, 2300, 1800, 1800, 2400

5.1. Simulation for Changed Road Surface Coefficient

The vehicle running condition on the changed road surface is set as follows: firstly, the vehicle is accelerated to 30 km/h and kept running on the road with the adhesion coefficient $\mu_{max} = 1.17$. From 20 s, the speed begins to increase to 100 km/h and is maintained for a period of time. Simultaneously, the road adhesion coefficient changes to $\mu_{max} = 0.2$. For comparison, three slip control algorithms: the PID control method, SMC (the control gain is set as 141) and the proposed HLQR method are simulated and analyzed. For all of the three slip control methods, the torque distribution algorithm is the same QP method as described in Section 4.

The vehicle speed controlled by the three slip control methods is demonstrated in Figure 5. It can be seen that the speed controlled by all three methods can reach the reference value within 20 s. After 20 s, the HLQR and SMC methods can control the vehicle speed with a smaller error than the PID method. During 20–30 s, the HLQR method can reach the fastest response for vehicle speed tracking.

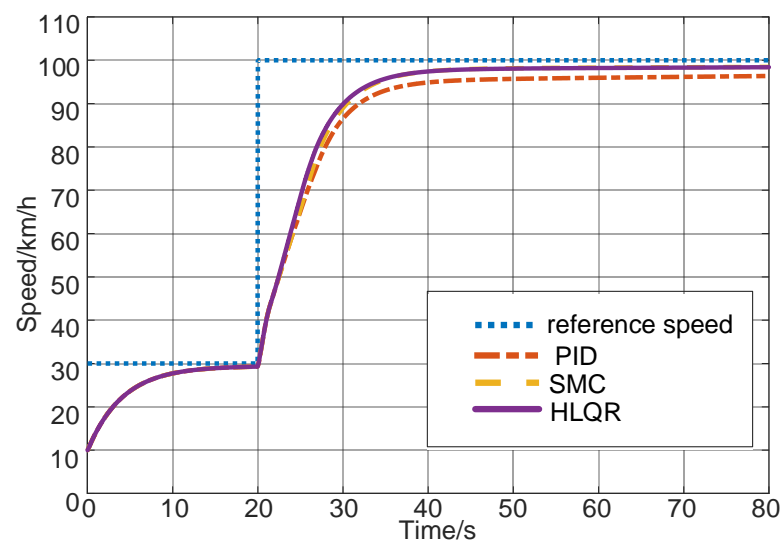


Figure 5. Vehicle speed on the changed road surface controlled by PID/SMC and HLQR.

The total driving torque is given in Figure 6a. The driving torque of the representative wheels controlled by the three slip control methods is demonstrated in Figure 6b–d. Because of the same road surface for the left and right wheels of one axle, there is no difference between the results of the two wheels. Therefore, the torque of three wheels: the left wheel of axle 1(1L), axle 3(3L), and axle 6(6L), are selected for analysis. It can be seen that the wheel torque distribution is conducted according to the cost functions to satisfy the total driving torque demand within 20 s. During this period, the anti-skid control is not active. The results of the PID control method, the SMC method, and the HLQR method are exactly the same because they use the same torque control allocation method. After 20 s, the road is changed to the low-adhesion surface. Especially, the vehicle needs to accelerate to 100 km/h as soon as possible during 20–30 s, which causes the large driving torque demand as shown in Figure 6a. As a result, the wheels on axle 3 and axle 6 slip, and the wheel torque is controlled by three different slip control algorithms. Then the vehicle accelerates close to 100 km/h, the driving torque requirement decreases, and the anti-slip control exits. Although the anti-slip control is not active before 20 s and after 30 s, the target vehicle speed and the tracking error are different. As a result, the demand for the total driving torque and the wheel torque is different after 30 s from that before 20 s.

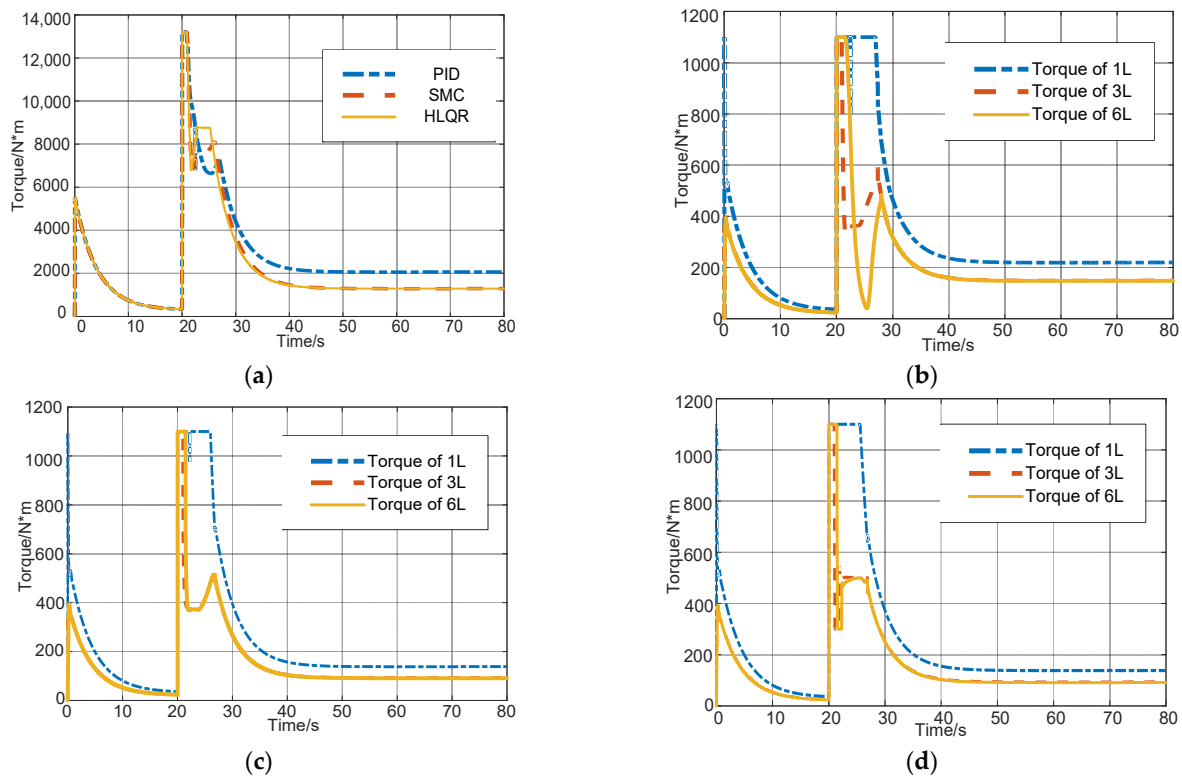


Figure 6. On the changed road surface: (a) total driving torque; torque of left wheel for the 1st, 3rd, and 6th axles; (b) controlled by PID; (c) controlled by SMC; (d) controlled by HLQR.

The wheel slip ratio controlled by the PID, SMC, and HLQR algorithms is shown in Figures 7–9, respectively. In each figure, the slip ratios of wheels 1 L, 3 L, and 6 L are presented. The results indicate that the vehicle accelerates and drives from the high adhesion road to the low adhesion road in 20 s. Then, the slip ratios of the 3rd axle and 6th axle increase sharply. Anti-skid control is activated based on the optimal slip ratio calculation. Then, the torque distribution results are constrained by the slip control results. However, it should be noted that the actual moment when each anti-skid control method is triggered and turned off is not exactly the same. This is because the difference between the actual vehicle speed and the total driving torque demand requires different control algorithm, as shown in Figures 5 and 6a. As presented in Figures 7a, 8a and 9a, there is no slip on the wheels of the 1st axle. As the optimal slip ratio on the maximum driving coefficient is not calculated when the anti-slip control is not active, the reference slip ratio of wheel 1 L is maintained at the default value of 0.17, which is the optimal slip ratio on the high adhesion coefficient road. As the anti-slip control is not active, the slip ratio of 1L does not need to be controlled to the reference value.

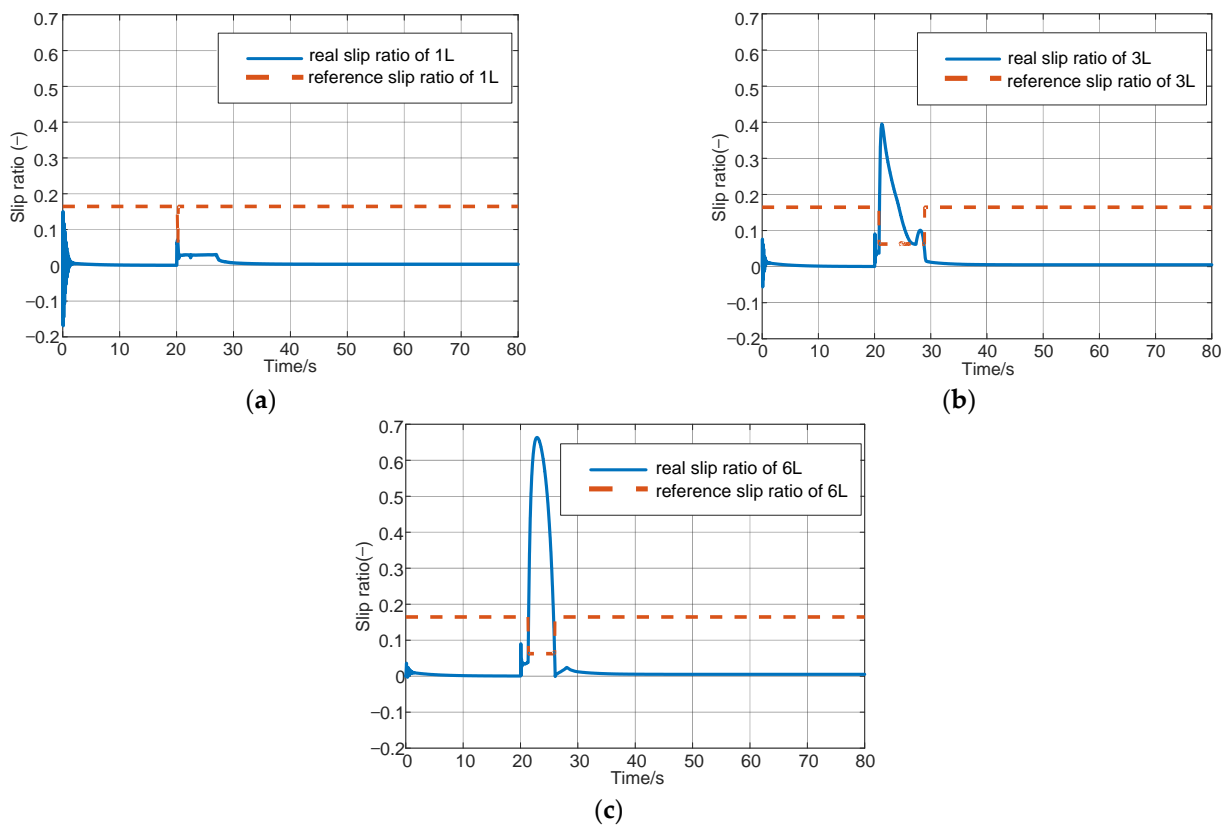


Figure 7. Slip ratio controlled by the PID method on the changed road surface: (a) left wheel of the 1st axle (1L); (b) left wheel of the 3rd axle (3L); (c) left wheel of the 6th axle (6L).

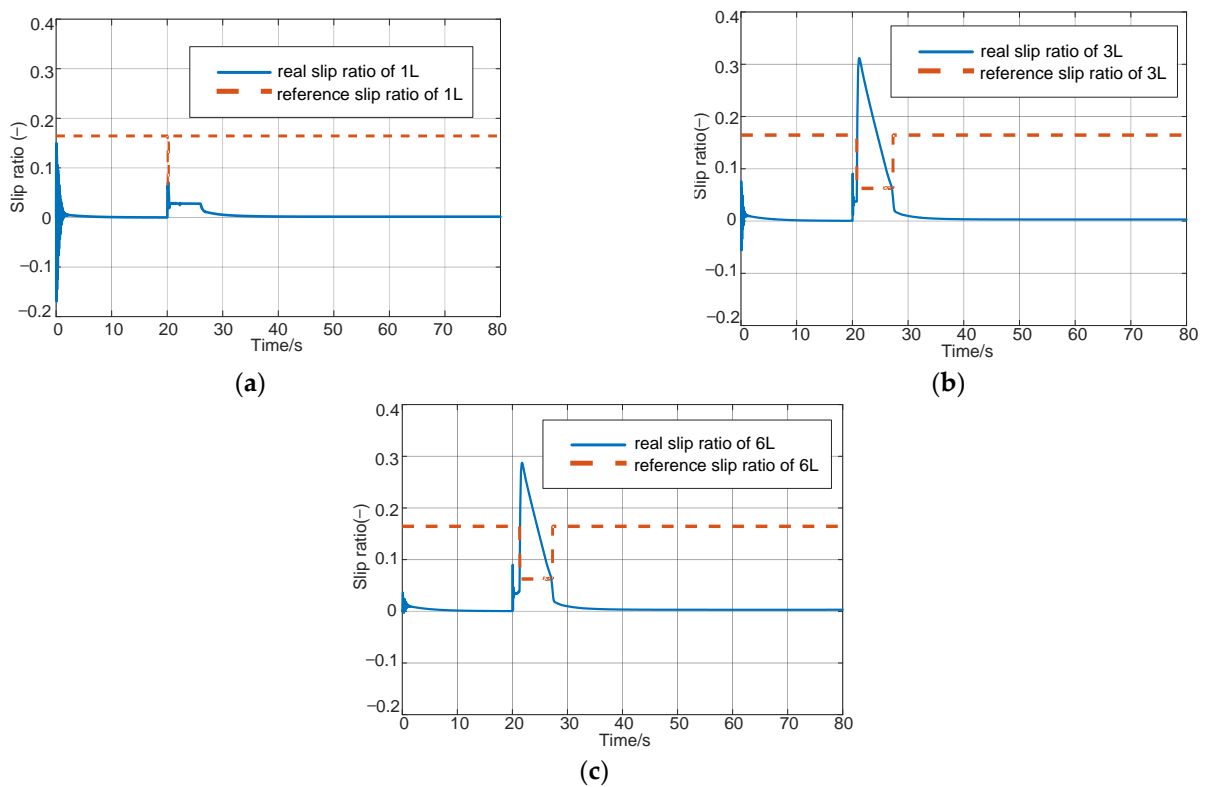


Figure 8. Slip ratio controlled by the SMC method on the changed road surface: (a) left wheel of the 1st axle (1L); (b) left wheel of the 3rd axle (3L); (c) left wheel of the 6th axle (6L).

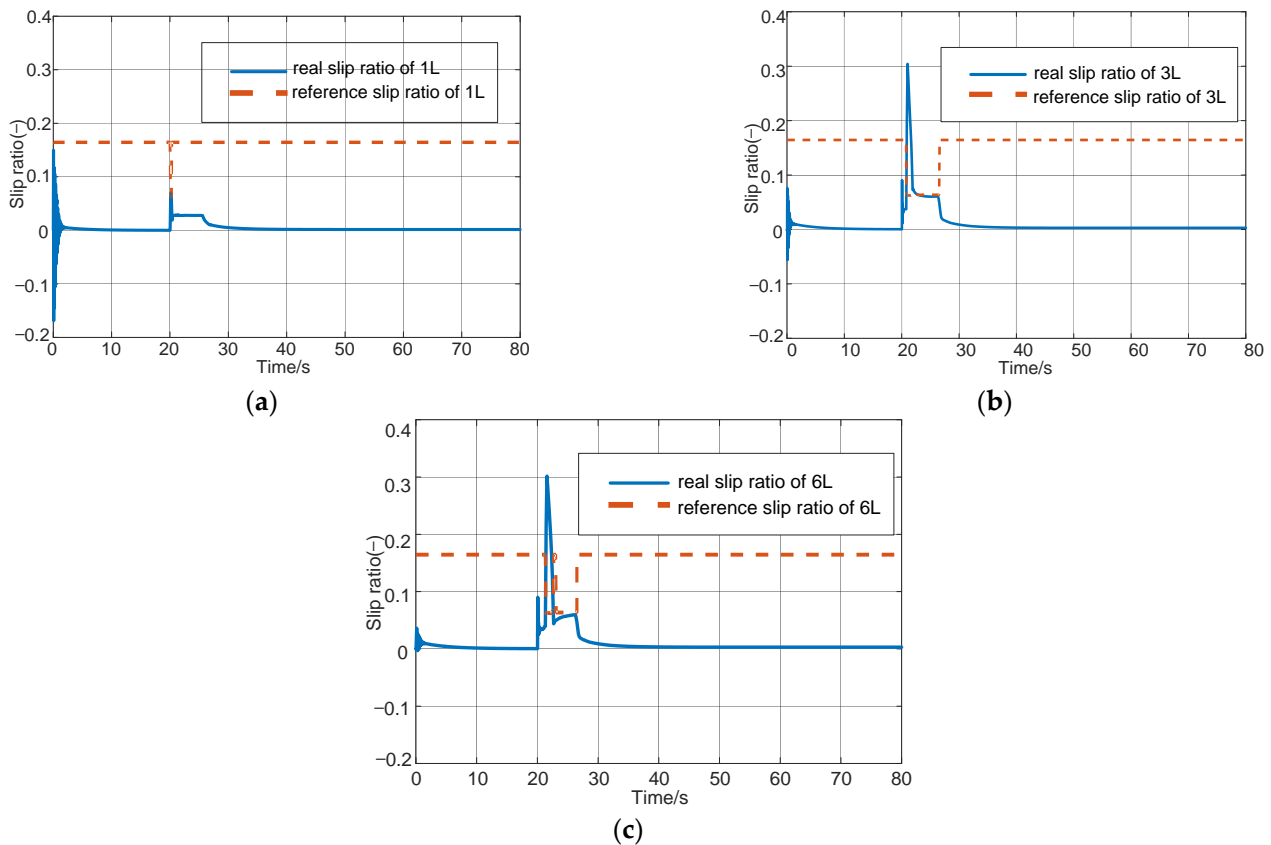


Figure 9. Slip ratio controlled by the HLQR method on the changed road surface: (a) left wheel of the 1st axle (1L); (b) left wheel of the 3rd axle (3L); (c) left wheel of the 6th axle (6L).

Figures 7b, 8b and 9b show the slip ratio of the left wheel for axle 3. As the anti-skid control of these wheels is active, the reference slip ratio is changed to 0.07, which is the optimal slip ratio on the low adhesion coefficient road. The wheel slip ratio is controlled to track the reference value by the PID, SMC, and HLQR algorithms. Due to the sudden change in road surface and large acceleration demand, all three control algorithms control the slip ratio with overshoot. This will cause the wheel to continue slipping before returning to stability. However, the overshoot and tracking error obtained by HLQR are smaller than those controlled by the other two methods. HLQR can track the reference slip ratio in 0.6 s, which is acceptable for vehicle dynamics safety. The root mean square (RMS) error of the slip ratio controlled by PID is 0.1751, SMC is 0.1502, which is decreased to 0.0675 by the HLQR control. Compared with PID and SMC control methods, HLQR can improve the accuracy of slip ratio control by 61.4% and 55.1%.

Figures 7c, 8c and 9c show the slip ratio of the left wheel for axle 6. Similarly, the wheel slips on the low-adhesion road, and the reference slip ratio changes to 0.07. The slipping of the 6th axle can be inhibited by the PID method. However, the slip rate is still large, and the stability of the wheels is poor. The SMC method can limit slip ratio, but the tracking error is larger and the response time is longer than that controlled by HLQR. The slip ratio is well controlled by the HLQR algorithm, and the wheel keeps stable. Similar to the wheel of 3L, the overshoot and tracking error obtained by HLQR are smaller than those controlled by the other two methods. The root mean square (RMS) error of the slip ratio controlled by PID is 0.4451 and the SMC is 0.1372, which is decreased to 0.0872 by the HLQR control. Compared with PID and SMC control methods, HLQR can improve the accuracy of slip ratio control by 80.4% and 36.4%.

From the above slip control results, the following conclusion could be drawn: the torque control allocation can be combined with the anti-slip control. If the anti-slip control is triggered, the torque distribution results are limited by the slip control results to ensure wheel dynamics stability. Compared with the PID slip control method and SMC, the HLQR can increase the accuracy of the slip ratio control.

5.2. Simulation on Split Road Surface with the Electric Motor Failure

To further verify the proposed control algorithm, a split road case with an electric motor failure is configured for simulation. As in Section 5.1, the vehicle is accelerated to 30 km/h and kept running on the road with an adhesion coefficient $\mu_{max} = 1.17$. From 20 s, the speed began to increase to 100 km/h and was maintained for a period of time. Simultaneously, the road adhesion coefficient changes to split road ($\mu_{max} = 1.17$ on the left side and $\mu_{max} = 0.2$ on the right side). When the vehicle is working on the split road, the left motor of the 1st axle fails with a failure factor $e_{11} = 0.5$ at 21 s. Then, at 23 s, the left motors of the 5th axle and 6th axle fail with a factor of $e_{10} = e_{12} = 0.2$.

Similarly, the vehicle speed controlled by the three slip control algorithms is demonstrated in Figure 10. The target speed and the vehicle control performance are essentially the same as the results in Section 5.1.

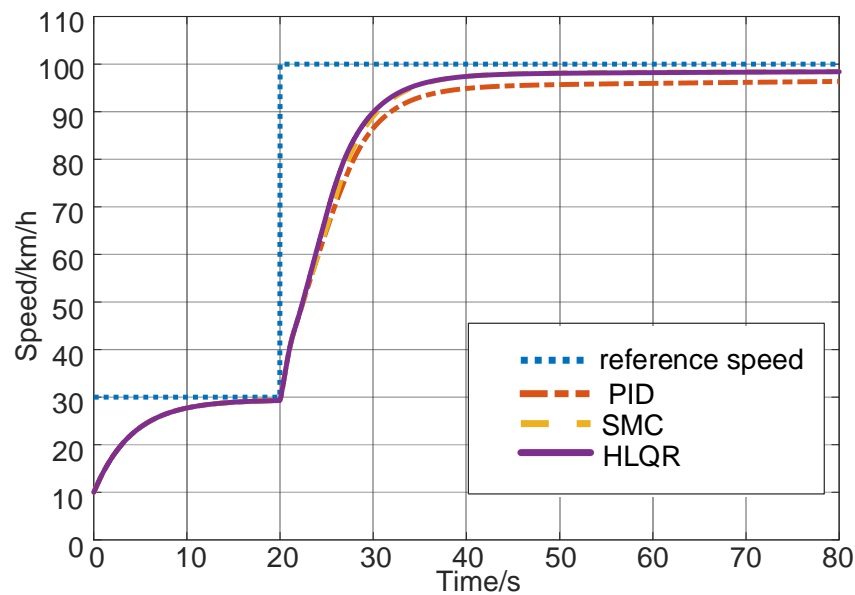


Figure 10. Vehicle speed on the split road surface controlled by PID/SMC and HLQR.

The torque of the left wheel for axle 1 (1 L), axle 3 (3 L), and axle 6 (6 L) is shown in Figure 11. From 21 s, the torque of the 1L starts to decrease because of electric motor failure. From 23 s, the torque of the 6L starts to decrease too. To satisfy the overall desired driving force, the torque of the 3rd axle increases to compensate for the decreased torque output of failed electric motors. In spite of the failure of some driving motors, the speed can reach the target speed, as shown in Figure 10. As the target speed is the presentation of the driver’s demand, it is indicated that the proposed control allocation method can satisfy the drivers’ demand.

Under this working condition, the right wheel enters the low-adhesion road and may slip. The left motor partially fails, but the wheel does not slip because of the high adhesion coefficient. Therefore, take the sliding wheel and the right wheel of axle 3 (3R) as examples to explain the effectiveness of algorithms. The slip ratios of 3R controlled by PID, SMC, and HLQR are presented in Figure 12. It can be seen that the wheel on the right side of the 3rd axle is well controlled and approaches the reference value by the HLQR algorithm with a smaller deviation. The RMS of the slip ratio controlled by the PID is 0.1634; that controlled by the SMC is 0.1156; and that controlled by the HLQR is 0.0983. Compared with PID and SMC control methods, HLQR can improve the accuracy of slip ratio control by 39.8% and 14.9%, respectively.

The slip ratio results of Sections 5.1 and 5.2 are summarized in Table 2. Compared with the PID and SMC slip control methods, the HLQR can increase the control accuracy of the slip ratio under various driving conditions. Through HLQR control, the RMS slip ratio can be decreased by more than 30%.

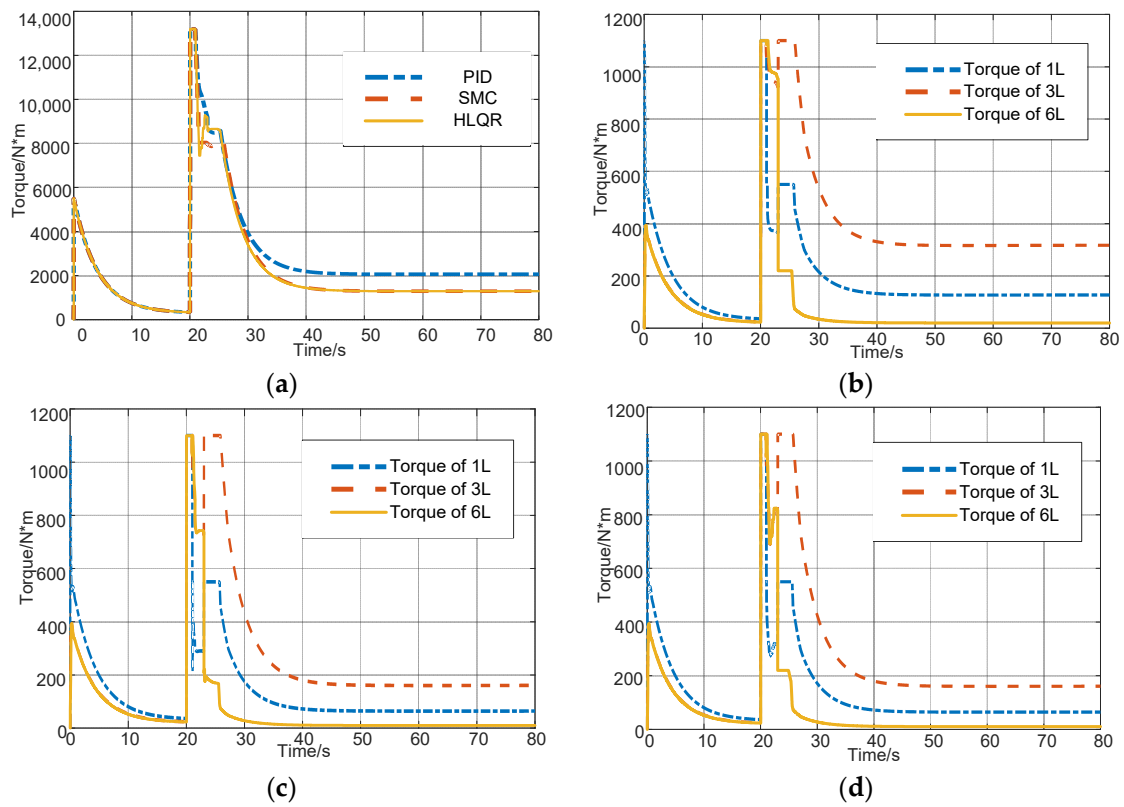


Figure 11. On the split road surface: (a) total driving torque; torque of left wheel for the 1st, 3rd; and 6th axes; (b) controlled by PID; (c) controlled by SMC; (d) controlled by HLQR.

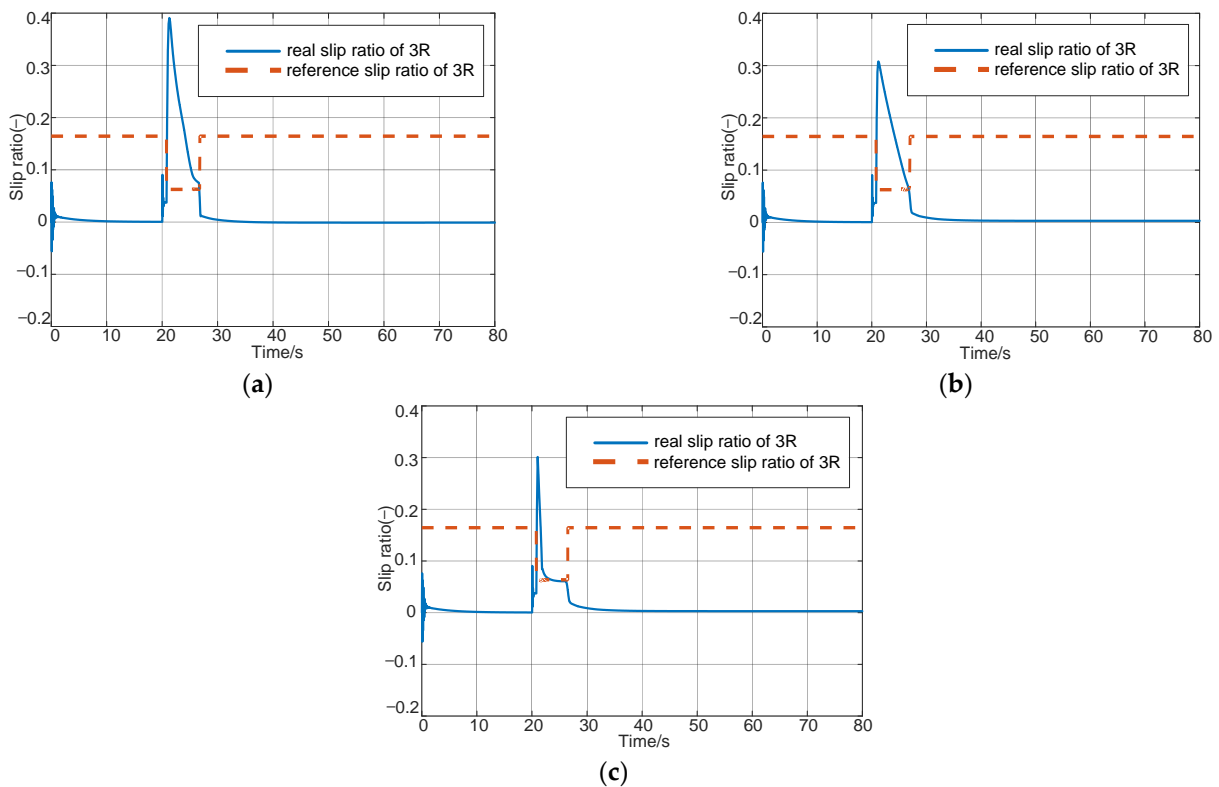


Figure 12. Slip ratio of the right wheel of the 3rd axle (3R) on the split road surface controlled by the (a) PID method, (b) SMC, and (c) HLQR.

Table 2. Comparison of the slip ratio RMS controlled by PID, SMC, and HLQR.

Algorithm	3L Changed Road	6L Changed Road	3R Split Road
PID	0.1751	0.4451	0.1634
SMC	0.1502	0.1372	0.1156
HLQR	0.0675	0.0872	0.0983
$\Delta RMS_{HLQR-PID}(\%)$	61.4	80.4	39.8
$\Delta RMS_{HLQR-SMC}(\%)$	55.1	36.4	14.9

From the control results for the electric motor failure condition, it can be concluded that the torque control allocation can be regulated to satisfy the driver's demand. Combined with slip control, the torque of wheels with a small slip ratio can be increased to compensate for the lost torque of the failed wheels. The torque distribution results are always limited by the slip control results to ensure wheel dynamic stability.

6. Discussion

This paper discusses designing a comprehensive scheme of longitudinal dynamics control for a 12×12 MADD vehicle based on the coordinated control of anti-slipping control and torque control allocation. Extensive simulations of different driving conditions are conducted. The results indicate that the proposed coordinated slip control based on HLQR is practical and efficacious and improves slip control accuracy compared with the PID and SMC methods. In addition, combined with slip control, torque control allocation can be adapted to cases of motor failure and wheel slipping. Limited by the slip control results to ensure wheel dynamic stability, the driving force can be distributed to satisfy the driver's demand as expected.

This paper expands the HLQR algorithm to multi-axle vehicles and simplifies the complexity of the vehicle longitudinal dynamics control system, which is an important contribution to the development of multi-axle vehicles. However, the local subsystems are decoupled only according to the wheel load in this paper. In future works, the impact of the road friction coefficient and road unevenness for each wheel can be further considered in the HLQR scheme. Furthermore, more tests on the real-time test bench and real MADD vehicle will be applied to verify the performance of the HLQR algorithm.

Author Contributions: Conceptualization, Y.B., C.D., D.W. and W.L.; Methodology, Y.B. and C.D.; Software, H.L.; Validation, C.D., Y.B. and D.W.; Formal Analysis, C.D. and Y.B.; Resources, C.D. and J.L.; Data Curation, H.L.; Writing—Original Draft Preparation, C.D. and Y.B.; Writing—Review and Editing, D.W., H.L. and W.L.; Visualization, H.L.; Supervision, C.D. and J.L.; Project Administration, C.D.; Funding Acquisition, C.D. All authors have read and agreed to the published version of the manuscript.

Funding: This research was funded by the National Natural Science Foundation of China (51975434, 51705383). The APC was funded by the National Natural Science Foundation of China (51975434).

Data Availability Statement: The data presented in this study are available upon request from the corresponding authors.

Conflicts of Interest: The authors declare no conflict of interest.

References

- Chen, H.; Gong, M.-D.; Zhao, D.-X.; Liu, W.-B.; Jia, G.-Y. Coordination Control of Multi-Axis Steering and Active Suspension System for High-Mobility Emergency Rescue Vehicles. *Mathematics* **2022**, *10*, 3562. [CrossRef]
- Hamouda, M.; Al-Amyal, F.; Odinaev, I.; Ibrahim, M.N.; Számel, L. A Novel Universal Torque Control of Switched Reluctance Motors for Electric Vehicles. *Mathematics* **2022**, *10*, 3833. [CrossRef]
- Yu, H.; Zhang, F.; Xi, J.; Cao, D. Mixed-Integer Optimal Design and Energy Management of Hybrid Electric Vehicles with Automated Manual Transmissions. *IEEE Trans. Veh. Technol.* **2020**, *69*, 12705–12715. [CrossRef]
- Gao, L.; Xiong, L.; Xia, X.; Lu, Y.; Yu, Z.; Khajepour, A. Improved Vehicle Localization Using On-Board Sensors and Vehicle Lateral Velocity. *IEEE Sens. J.* **2022**, *22*, 6818–6831. [CrossRef]
- Chen, H.; Lian, X.; Lyu, C. Piecewise integral-proportional wheel slip control for an in-wheel motor driven vehicle. *Veh. Syst. Dyn.* **2022**, 1–21. [CrossRef]

6. Zhang, L.; Chen, H.; Huang, Y.; Wang, P.; Guo, K. Human-Centered Torque Vectoring Control for Distributed Drive Electric Vehicle Considering Driving Characteristics. *IEEE Trans. Veh. Technol.* **2021**, *70*, 7386–7399. [[CrossRef](#)]
7. Hua, M.; Chen, G.; Zhang, B.; Huang, Y. A hierarchical energy efficiency optimization control strategy for distributed drive electric vehicles. *Proc. Inst. Mech. Eng. Part D J. Automob. Eng.* **2018**, *233*, 605–621. [[CrossRef](#)]
8. George, A.D.; Besselink, I. Rear suspension design for an in-wheel-drive electric car. *Proc. Inst. Mech. Eng. Part D J. Automob. Eng.* **2015**, *230*, 147–159. [[CrossRef](#)]
9. Zhao, B.; Gao, F.; Tian, L. Normalized coupling method for speed synchronization of multi-axis driving vehicles. *Int. J. Adv. Robot. Syst.* **2012**, *9*, 50.
10. Trikande, M.; Karve, N.; Rajamohan, V.; Jagirdar, V.; Vasudevan, R. Semi-active vibration control of an 8x8 armored wheeled platform. *J. Vib. Control* **2016**, *24*, 283–302. [[CrossRef](#)]
11. Hashemi, E.; Jalali, M.; Khajepour, A.; Kasaiezadeh, A.; Chen, S.-K. Vehicle Stability Control: Model Predictive Approach and Combined-Slip Effect. *IEEE/ASME Trans. Mechatron.* **2020**, *25*, 2789–2800. [[CrossRef](#)]
12. Xia, X.; Xiong, L.; Lu, Y.; Gao, L.; Yu, Z. Vehicle sideslip angle estimation by fusing inertial measurement unit and global navigation satellite system with heading alignment. *Mech. Syst. Signal Process.* **2021**, *150*, 107290. [[CrossRef](#)]
13. Xia, X.; Xiong, L.; Leng, B.; Yu, Z. Vehicle stability control based on driver's emergency alignment intention recognition. *Int. J. Automot. Tech.* **2017**, *18*, 993–1006.
14. Kim, W.; Yi, K.; Lee, J. An optimal traction, braking, and steering coordination strategy for stability and manoeuvrability of a six-wheel drive and six-wheel steer vehicle. *Proc. Inst. Mech. Eng. Part D J. Automob. Eng.* **2011**, *226*, 3–22. [[CrossRef](#)]
15. Xia, X.; Hashemi, E.; Xiong, L.; Khajepour, A. Autonomous Vehicle Kinematics and Dynamics Synthesis for Sideslip Angle Estimation Based on Consensus Kalman Filter. *IEEE Trans. Control. Syst. Technol.* **2022**, *31*, 179–192. [[CrossRef](#)]
16. Liu, M.C.; Zhang, C.N. Development of an optimal control system for longitudinal and lateral stability of an individual eight-wheel-drive electric vehicle. *Int. J. Veh. Des.* **2015**, *69*, 132. [[CrossRef](#)]
17. Hu, J.; Li, J.; Hu, Z.; Zhang, B.; Xu, L.; Ouyang, M. Energy-efficient torque-allocation strategy for a 6×6 vehicle using electric wheels. *Etransportation* **2021**, *5*, 100136. [[CrossRef](#)]
18. Han, Z.; Xu, N.; Chen, H.; Huang, Y.; Zhao, B. Energy-efficient control of electric vehicles based on linear quadratic regulator and phase plane analysis. *Appl. Energy* **2018**, *213*, 639–657. [[CrossRef](#)]
19. Grechi, S.; Caiti, A. Comparison between Optimal Control Allocation with Mixed Quadratic & Linear Programming Techniques. *IFAC-PapersOnLine* **2016**, *49*, 147–152. [[CrossRef](#)]
20. Wang, Z.; Ding, X.; Zhang, L. Overview on Key Technologies of Acceleration Slip Regulation for Four-wheel-independently-actuated Electric Vehicles. *J. Mech. Eng. Chin. Ed.* **2019**, *55*, 99–120.
21. Chen, G.; He, L.; Zhang, B.; Hua, M. Dynamics integrated control for four-wheel independent control electric vehicle. *Int. J. Heavy Veh. Syst.* **2019**, *3–4*, 515–534. [[CrossRef](#)]
22. Yan, Y.; Zhang, Y.; Yan, N. Research on acceleration slip regulation of 6x6 electrically-driven wheeled vehicle. *Acta Armamentarii* **2014**, *35*, 1335–1343.
23. Chen, G.; Hua, M.; Zong, C.; Zhang, B.; Huang, Y. Comprehensive chassis control strategy of FWIC-EV based on sliding mode control. *IET Intell. Transp. Syst.* **2019**, *13*, 703–713. [[CrossRef](#)]
24. Liu, L.; Fei, J.; Yang, X. Adaptive Interval Type-2 Fuzzy Neural Network Sliding Mode Control of Nonlinear Systems Using Improved Extended State Observer. *Mathematics* **2023**, *11*, 605. [[CrossRef](#)]
25. Cai, L.; Liao, Z.; Wei, S.; Li, J. *Improvement of Maneuverability and Stability for Eight Wheel Independently Driven Electric Vehicles by Direct Yaw Moment Control*; ICEMS: Gyeongju, Republic of Korea, 2021. [[CrossRef](#)]
26. Xia, X.; Xiong, L.; Huang, Y.; Lu, Y.; Gao, L.; Xu, N.; Yu, Z. Estimation on IMU yaw misalignment by fusing information of automotive onboard sensors. *Mech. Syst. Signal Process.* **2021**, *162*, 107993. [[CrossRef](#)]
27. Nguyen, D.-H.; Hara, S. Hierarchical Decentralized Controller Synthesis for Heterogeneous Multi-Agent Dynamical Systems by LQR. *SICE J. Control. Meas. Syst. Integr.* **2015**, *8*, 295–302. [[CrossRef](#)]
28. Sadamoto, T.; Ishizaki, T.; Imura, J.-I. *Hierarchical Distributed Control for Networked Linear Systems*; CDC: Los Angeles, CA, USA, 2014; pp. 2447–2452. [[CrossRef](#)]
29. Nguyen, B.-M.; Hara, S.; Fujimoto, H.; Hori, Y. Slip control for IWM vehicles based on hierarchical LQR. *Control Eng. Pract.* **2019**, *93*, 104179. [[CrossRef](#)]
30. Liu, W.; Xia, X.; Xiong, L.; Lu, Y.; Gao, L.; Yu, Z. Automated vehicle sideslip angle estimation considering signal measurement characteristic. *IEEE Sens. J.* **2021**, *19*, 21675–21687. [[CrossRef](#)]
31. Liu, W.; Quijano, K.; Crawford, M.M. YOLOv5-Tassel: Detecting tassels in RGB UAV imagery with improved YOLOv5 based on transfer learning. *IEEE J. Sel. Top. Appl. Earth Obs. Remote Sens.* **2022**, *15*, 8085–8094. [[CrossRef](#)]
32. Burckhardt, M. *Wheel Slip Control Systems*; Vogel Verlag: Würzburg, Germany, 1993.

Disclaimer/Publisher's Note: The statements, opinions and data contained in all publications are solely those of the individual author(s) and contributor(s) and not of MDPI and/or the editor(s). MDPI and/or the editor(s) disclaim responsibility for any injury to people or property resulting from any ideas, methods, instructions or products referred to in the content.